Length-Dependent Plasmon Resonance in Single-Walled Carbon Nanotubes

Takahiro Morimoto,[†] Soon-Kil Joung,[†,‡] Takeshi Saito,[†,‡] Don N. Futaba,[†,‡] Kenji Hata,[†,‡] and Toshiya Okazaki*[,†,‡]

[†]Technology Research Association for Single Wall Carbon Nanotubes (TASC), Tsukuba 305-8565, Japan and [‡]Nanotube Research Center, National Institute of Advanced Industrial Science and Technology (AIST), Tsukuba 305-8565, Japan

ABSTRACT The optical response of single-walled carbon nanotubes (SWCNTs) to far-infrared (FIR) radiation was systematically studied using various SWCNTs with different tube-length distributions. The observed peak position in the FIR spectra linearly scaled with the inverse of tube length irrespective of diameter, which is consistent with the dispersion relation predicted by the one-dimensional plasmon resonance model. The effects of chemical doping on the FIR spectra of the separated metallic and semiconducting SWCNTs clearly indicate that the motion of plasmons in the electronic band structures is primarily responsible for the optical response in these spectral regions. The observed absorption peaks are naturally sensitive to the presence of defects on the tube wall and correlated with the electric resistance, suggesting that the plasmons resonate with the current path length of the SWCNTs.

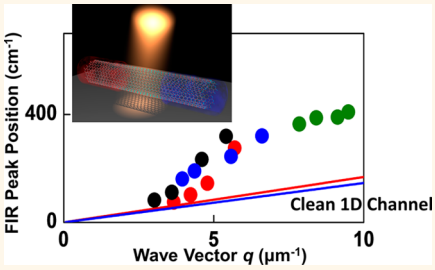

KEYWORDS: carbon nanotubes · plasmon · far-infrared spectroscopy

Single-walled carbon nanotubes (SWCNTs) are promising one-dimensional (1D) carbon materials.[1] The confinement of electrons in the radial direction leads to unusual quantum effects on their electronic properties.[2,3] For instance, SWCNTs exhibit very unique optical properties associated with their low dimensionality over a wide spectral range. In the ultraviolet−visible−near-infrared (UV−vis−NIR) region, sharp transition peaks are observed, which are related to the interband transitions between 1D van Hove singularities.[4] On the other hand, a broad absorption peak is observed in the UV region, which can be attributed to the π-plasmon collective excitation of SWCNTs.[5,6]

Furthermore, in the far-infrared (FIR) frequency ranges, there is a broad absorption peak at a frequency on the order of 100 cm^{-1}.[7−19] This feature was first reported more than 10 years ago and was ascribed to the narrow gap of metallic SWCNTs.[20] The finite radial curvature of SWCNTs induces a shift of the Fermi point from the original K point, leading to small energy gaps near the Fermi level of metallic SWCNTs. The induced narrow gap has actually been observed *via* low-temperature scanning tunneling spectroscopy in the energy region on the order of 10 meV, which corresponds to the FIR frequencies (on the order of 100 cm^{-1}).[21] Importantly, this narrow gap exhibits strong diameter dependence; that is, the gap energy is inversely proportional to the square of the tube diameter.[22−24]

An alternative interpretation of the optical response in the FIR region is the plasmon excitation of SWCNTs of finite tube length.[9,12,13,17−19] The confined free carriers in metallic SWCNTs interact with the low-frequency electric field, resulting in intense optical absorption. However, the detailed mechanisms of the low-dimensional plasmon in both SWCNTs and graphene[25−27] have so far remained unclear because the plasmonic excitation is highly sensitive to their conductive length, band structures, and dimensionalities.[12,28] Therefore, the systematic study of the FIR spectroscopy is strongly demanded by the well-prepared SWCNT samples. Specifically, because plasmonic motion in 1D nanostructures should be sensitive to the conductive path length,

* Address correspondence to toshi.okazaki@aist.go.jp.

Received for review January 16, 2014 and accepted October 5, 2014.

Published online October 06, 2014
10.1021/nn505430s

it is highly desirable that such spectroscopic measurements be performed using SWCNTs with different tube lengths but a constant diameter.

Here, we report the FIR spectroscopic study of various SWCNT samples of different tube lengths. Each SWCNT was cut *via* strong sonication with a different duration. Importantly, the sonication processes did not affect the diameter distribution, which was confirmed using resonance Raman and UV−vis−NIR absorption spectroscopy. The obtained FIR absorption frequencies of clean and long SWCNTs exhibited quantitative agreement with the 1D plasmon dispersion relation. Moreover, the different effects of doping on the FIR spectra between metallic and semiconducting SWCNTs indicate that the motion of the photoinduced carriers predominantly accounts for the optical response. It was also found that the observed resonance peaks were very sensitive to the presence of defects on the tube wall and correlated with the electric resistance of the samples. These observations suggest that the 1D current path length of the SWCNTs determines the plasmon resonance conditions.

RESULTS

FIR Spectroscopy of SWCNTs with Different Tube Lengths. Figure 1a shows the histograms of the length distributions of the SWCNTs, which were synthesized using the electric-arc-discharging method (arc-SWCNTs) after several different sonication processes (top to bottom: 10 min, 20 min, 1 h, and 3 h), as estimated from AFM observations. For 10 min of sonication, the average tube length (median value) was estimated to be 0.86 μm. The average tube length decreased with increasing sonication time. The average tube length finally became 0.55 μm after 3 h of sonication.

We checked that the applied sonication processes did not affect the diameter distributions of the SWCNT samples using resonance Raman and absorption spectroscopy. Figure 1b shows the resonance Raman spectra of the processed samples with 532 nm laser excitations. A prominent peak of the radial breathing mode (RBM) was observable at approximately 175 cm^{-1}, which corresponds to a diameter of $d_t \sim 1.4$ nm.[29] It can be clearly seen that the RBM shapes and peak positions are nearly identical for all sonication processes.

Figure 1c shows the optical absorption spectra of the SWCNT samples on quartz substrates with different sonication times. In this energy region, the first and second interband transitions for the semiconducting SWCNTs (S1 and S2) and the first interband transition for the metallic SWCNTs (M1) were observed at approximately 1800, 1000, and 700 nm, respectively. The peak positions and the spectral shapes are apparently insensitive to sonication duration. The absence of any

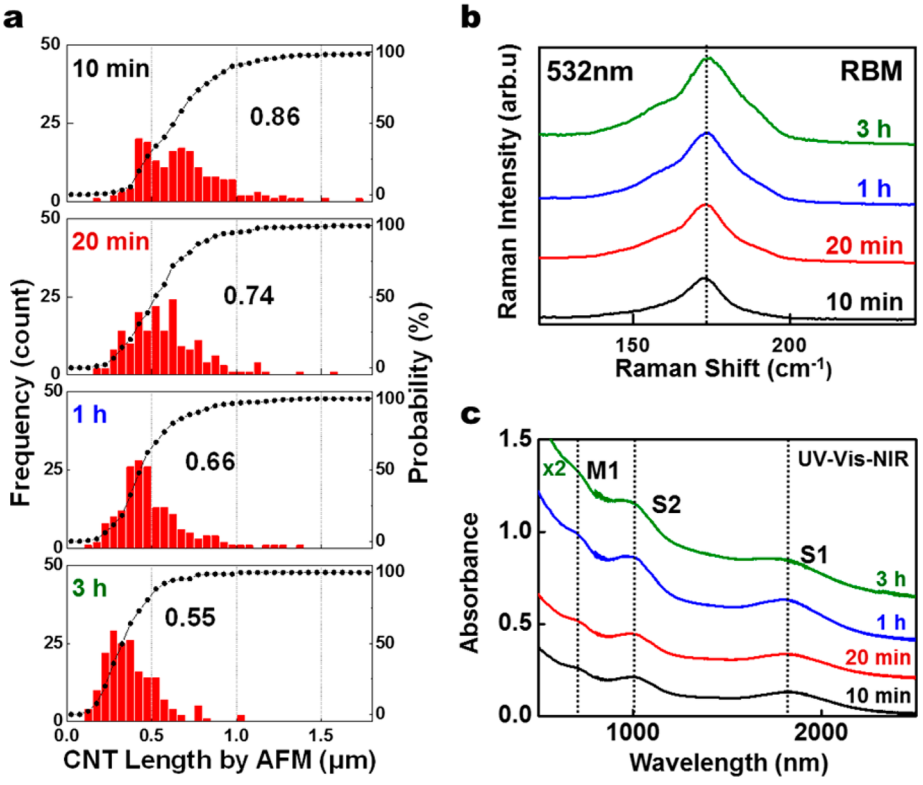

Figure 1. (a) Tube-length distributions of arc-SWCNTs based on AFM observations. Each panel shows the results for samples that correspond to different sonication times: from top to bottom, the sonication time was 10 min, 20 min, 1 h, and 3 h. The numbers inside the panels denote the median values of the distributions. (b) Resonance Raman excited by the 532 nm laser and (c) UV−vis−NIR absorption spectra of arc-SWCNTs with different sonication times. The dashed lines are guides for the eye. The baselines of the absorption spectra are adjusted.

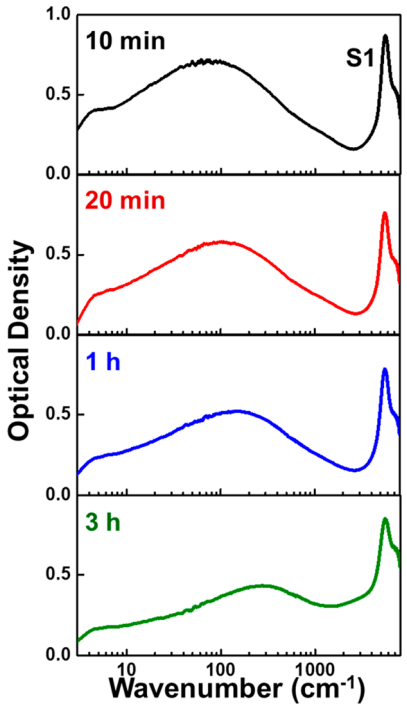

Figure 2. FIR spectra of arc-SWCNTs with different sonication times of 10 min, 20 min, 1 h, and 3 h (from top to bottom). The sharp peaks near 5500 cm^{-1} correspond to the S1 interband transition.

significant change in either the Raman spectrum or the absorption spectrum strongly suggests that the diameter and chiral-angle distributions of the arc-SWCNTs remained unchanged throughout all sonication processes.

The optical response in the FIR region exhibits significant sonication time dependence. Figure 2 shows the FIR optical density spectra of the arc-SWCNTs with different sonication times from 10 min to 3 h. The black line represents the FIR spectrum of the SWCNT sample that corresponds to 10 min of sonication. A broad and strong peak can be seen at approximately 70 cm^{-1}. As the duration increases, the peak maximum clearly shifts toward higher frequencies. For 3 h of sonication, the peak is located at approximately 270 cm^{-1}. Because the diameter and chiral-angle distributions are unchanged (Figure 1b,c), the observed shifts are unambiguously caused by the shortening in the tube length (Figure 1a) but not a curvature-induced narrow gap.

The same FIR spectroscopic experiments were also conducted for enhanced direct-injection pyrolytic synthesis (e-DIPS), HiPco, and supergrowth (SG) SWCNTs (see Supporting Information). For all of these SWCNTs, the FIR spectra were observed to shift toward higher wavenumbers as the tubes were shortened by the sonication process, while the diameter distributions remained unchanged. Figure 3a shows the relation between the observed FIR peak positions and the average tube length based on the AFM observations (L_{AFM}) for all investigated SWCNTs (see Figure 1a

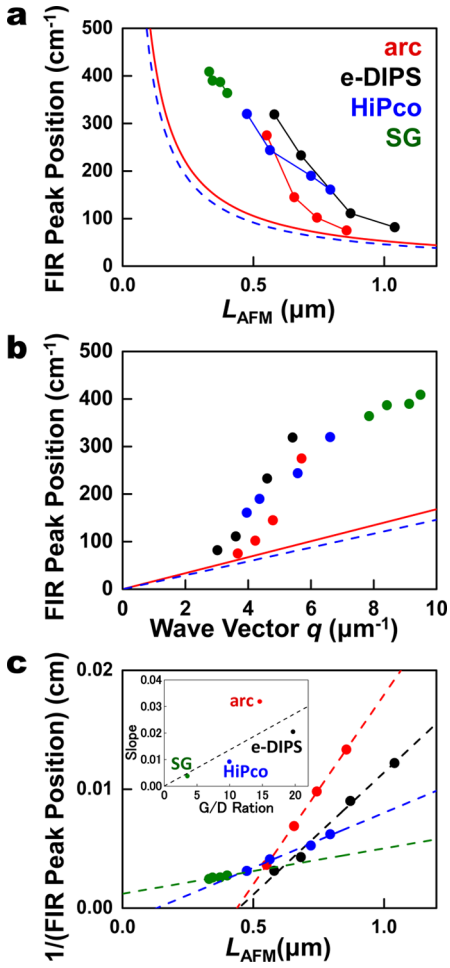

Figure 3. (a) Obtained FIR peak positions of arc- (red), e-DIPS (black), SG (green), and HiPco (blue) SWCNTs as a function of L_{AFM}. (b) Dispersion relation between the observed FIR peak position and the wave vector q ($=\pi/L_{AFM}$). The solid red and dashed blue lines in panels (a) and (b) are theoretical prediction curves for an ideal and clean SWCNT (see text) with 0.8 and 4.0 nm in diameter, respectively. (c) Inverse of the FIR peak position as a function of SWCNT length. (Inset) Slope of main panel as a function of G/D ratio from the short sonication time samples. The experimental errors of the FIR peak positions were less than 1%.

and Supporting Information). Despite the large difference in average tube diameter among these tubes (approximately 1.5, 2, 1, and 3 nm for arc-, e-DIPS, HiPco, and SG tubes, respectively), there is a good correlation between the obtained peak position and the average tube length.

Recently, Nakanishi and Ando formulated the optical response of finite-length metallic SWCNTs based on the 1D plasmon resonance model.[12] Because SWCNTs have considerably smaller diameters and longer coherent lengths than conventional metal systems, electrons on SWCNTs are strongly confined to the 1D channel.[30] For such mesoscopic-scale systems, a self-consistent approach with nonlocal and local conductivity was applied to model the dynamical response of their charge distributions.[12,31] The calculated results predict that the optical absorption should

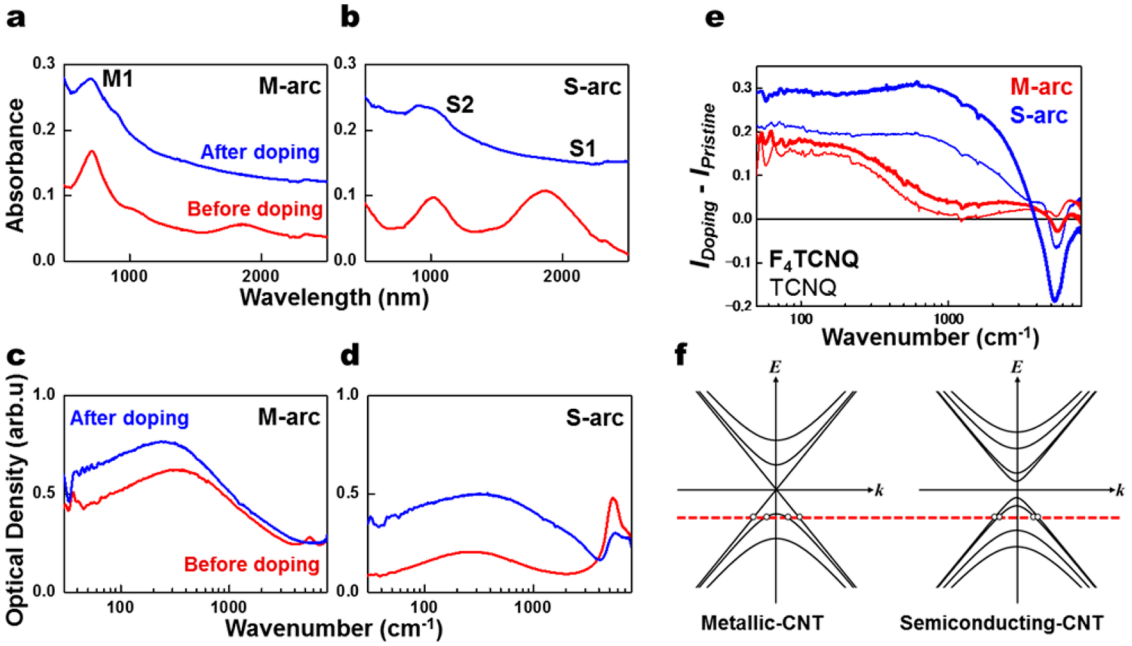

Figure 4. (a,b) UV−vis−NIR and (c,d) FIR spectra of (a,c) metallic- and (b,d) semiconducting-enriched arc-SWCNT samples. The red and blue lines are the spectra before and after F_4TCNQ doping, respectively. The UV−vis−NIR spectra (a) and (c) are offset in vertical axis. (e) Subtracted spectra of FIR intensities before and after doping for the M-arc (red) and S-arc (blue) samples. The bold and thin lines indicate the samples for which F_4TCNQ and TCNQ, respectively, were used as dopants. (f) Schematic illustrations of the band structures of metallic and semiconducting SWCNTs. The dashed red line corresponds to the Fermi energy level after chemical doping.

exhibit a resonant peak in the FIR regime.[12] The plasmon velocity is described as

$$v_P = 4v_F\sqrt{\frac{g_v g_s}{4}\frac{e^2}{2\pi\varepsilon\gamma}I_0(rq)K_0(rq)} \quad (1)$$

where v_P is the plasmon velocity, v_F is the Fermi velocity, g_v and g_s are degeneracies for the valley and spin, respectively, ε is the dielectric constant in the environment of SWCNTs, I_0 and K_0 are the modified Bessel function of the first and second kind, respectively, r is the radius of the SWCNT, q is the wavenumber given by $2\pi/L$, and γ is the band parameter.[12]

The peak position depends on the tube length, which is approximately defined as

$$\frac{2L}{v_P} = \frac{2\pi}{f}n \ (n = 1, 3, 5, \ldots) \quad (2)$$

where f is the frequency of the incident light.[12] If the tube length is sufficiently long that edge effects may be neglected, the resonance frequency f is inversely proportional to the length L. Indeed, the observed FIR peak frequencies exhibit the $1/L$ relation, as shown in Figure 3a. Moreover, within this model, the alignment between SWCNTs and incident light only has an effect on the intensity of the FIR peaks structures. In the previous works,[8,9,18] some groups reported significant changes of intensities of these FIR peaks in parallel and orthogonal conditions. These are consistent with the theoretical predictions.

The corresponding dispersion relation between f and the wave vector ($q = \pi/L_{AFM}$) for each SWCNT is shown in Figure 3b. When the induced current is severely impeded by impurities on the SWCNT channel, the dispersion curve rises nonlinearly with q.[12] The almost-linear relationship between the FIR peak position and the obtained q indicates that the plasmonic current travels along a relatively clean channel.[12,32,33] The observed divergence among the SWCNTs fabricated using different synthesis methods is discussed later.

Chemical-Doping Experiments on Separated SWCNTs. To better understand the basic features of the plasmonic resonance in SWCNTs, it is particularly helpful to investigate the optical response of SWCNTs with different electronic states. Therefore, chemical-doping experiments were also conducted on separated metallic and semiconducting SWCNTs using p-type dopants, tetrafluorotetracyanoquinodimethane (F_4TCNQ) and tetracyanoquinodimethane (TCNQ).[34] Figure 4a,b shows the UV−vis−NIR spectra of metallic-rich (M-arc) and semiconducting-rich (S-arc) arc-SWCNTs before and after doping with F_4TCNQ. Before doping, the sample films were annealed in vacuum (600 °C, approximately 10^{-5} Pa for 1 h) to remove adsorbed molecules such as oxygen and water. Both samples show clear interband excitation peaks at approximately 1800, 1000, and 700 nm, which correspond to the S1, S2, and M1 transitions, respectively (red lines in Figure 4a, b). Upon F_4TCNQ doping, the S1 peak disappears almost completely in the absorption spectrum (blue line in Figure 4b). The S2 and M1 peaks are also suppressed by the hole injection into the van Hove singularities in the valence bands.[35]

Figure 4c,d shows the effects of doping on the FIR spectra of the M-arc and S-arc samples. The red and blue lines denote the spectra before and after doping, respectively. The spectral intensities were normalized to the sample thicknesses that were estimated from AFM observations (see Methods). Before doping (red lines in Figure 4c,d), the FIR signal of the M-arc sample was considerably larger than that of the S-arc sample. The weaker but observable peak in the S-arc spectrum may originate from residual metallic SWCNTs in the S-arc sample and/or the doping of the semiconducting species by unexpected adsorbed molecules. Upon F_4TCNQ doping, the signal intensities of both the M-arc and S-arc samples were enhanced, which can be explained by the increase in the carrier density (blue lines in Figure 4c,d). Importantly, the signal enhancements observed upon doping appear to contradict the mini-gap model.

Even though the intensities increased in both cases, the details of the behavior differ significantly between the M-arc and S-arc samples. Apparently, the FIR spectrum of the S-arc sample increased equally across the observed frequency region, whereas the lower-frequency part was more enhanced in the M-arc sample. The subtracted spectra of the M-arc and S-arc samples were calculated to highlight the differences between the spectra before and after doping; these subtracted spectra are shown as the thick red and blue lines in Figure 4e, respectively. In fact, the subtracted spectrum of the S-arc sample shows a nearly constant increase, irrespective of frequency. However, in the M-arc sample, an increase is evident only in the lower-frequency part, and the intensity enhancement is smaller than that in the S-arc sample.

These behaviors can be clearly understood in terms of the carrier dynamics in the electronic band structures. Figure 4f shows schematic illustrations of the band structures of metallic and semiconducting SWCNTs. Metallic SWCNTs ideally exhibit a linear dispersion relation near the K point, while there is a band gap of approximately 1 eV for semiconducting SWCNTs. The Fermi level may be located near the Dirac point after vacuum annealing, resulting in the apparent interband transitions in the UV−vis−NIR absorption spectra (red lines in Figure 4a,b). Based on the UV−vis−NIR spectra, the Fermi levels in metallic and semiconducting SWCNTs are expected to shift downward to the dotted lines in Figure 4f upon F_4TCNQ doping. In the case of metallic SWCNTs, the new carriers were doped into the lowest parabolic band in addition to the linear dispersion band. Because of the finite curvature of the parabolic band, the doped carriers in this band should have a heavier effective mass and a slower Fermi velocity than those in the linear band. These slower carriers should experience a slightly longer effective tube length, resulting in the modification of the resonance condition toward lower frequencies (Figure 4c). In the case of semiconducting SWCNTs, however, the lowest two valence bands are nearer the $E = 0$ line than is the parabolic band of metallic SWCNTs with similar diameter. Therefore, the carriers in the linear band of the semiconducting SWCNTs have faster velocities than the carrier in the bottom of the parabolic band of metallic SWCNTs. Consequently, the spectral shape of the semiconducting SWCNTs remained unchanged (Figure 4d).

This phenomenon was more apparent when a weaker p-type dopant, TCNQ, was employed (thin lines in Figure 4e and Supporting Information). The enhancement in the lower-frequency range was stronger in the subtracted spectrum of the M-arc sample. Simultaneously, the spectral intensity remained almost unchanged in the higher-frequency range of >1000 cm^{-1}. In this case, the doped carriers have a heavier effective mass than in the F_4TCNQ case, so the slower carriers result in a much lower resonance frequency. These doping effects strongly indicate that the resonance conditions of the conductive carriers are important to understanding the optical response of SWCNTs in the FIR frequency region.

In the two-dimensional electron gas (2DEG) cavity system[36−38] and microribbon grapheme,[25−27] the excited collective plasmon frequency significantly depends on the carrier density n_c in the channel ($f \propto \sqrt{n_c}$ and $n_c^{1/4}$ for 2DEG and graphene, respectively). However, the effects of doping on the FIR spectroscopy of SWCNTs did not exhibit such a simple carrier-density dependence. Rather, the observed resonance conditions can be described in terms of the Fermi velocity of the carriers and the SWCNT length, as predicted by the 1D plasmon model.[12,28]

DISCUSSION

The present observations strongly suggest that the motion of the free carriers is responsible for the FIR signals of SWCNTs. Naturally, the induced current should be affected by the presence of defects and kinks on the SWCNT channel. The solid and dashed lines in Figure 3a,b are the curves calculated based on eq 1 with $2r = 0.8$ nm (smallest) and 4.0 nm (largest) assuming that $v_F = 0.8 \times 10^6$ m s^{-1}.[12,30] The small difference between two lines indicates that the diameter effect is quite small for the FIR peaks in this experiment.

If the current flows along the tube without scattering, the resonance frequency is ideally calculated based on the tube length using this relation. Although all samples have random orientation and contain some bundling SWCNTs, the results of relatively clean and long SWCNTs (arc- and e-DIPS SWCNTs for 10 min sonication processes) show good quantitative agreement with the theoretical predictions (Figure 3a,b). It is quite natural that the number of the defects increases with increasing sonication time, thereby the deviation

from the theoretical curves also increases. This suggests that the random orientation and the bundling effects might be small in the present experimental conditions.

Furthermore, there is substantial divergence in the observed FIR peak positions, even though almost identical L_{AFM} values were estimated (Figure 3a). For example, arc-SWCNTs and HiPco SWCNTs with nearly the same L_{AFM} of 730 nm show different FIR peak positions of approximately 102 and 190 cm^{-1}, respectively. This means that samples with the same L_{AFM} resonate at different frequencies, presumably because of the presence of defects or kinks in the SWCNT walls. If a SWCNT channel consists of some conductive paths affected by defects (or kinks), the "effective" length (L_{IR}) can be expressed as $L_{IR} = L_{AFM}/(N_{defect} + 1)$, where N_{defect} is the average number of the defects on a tube. Because the inverse of the FIR position is proportional to the conductive length (eq 2), the number of defect sites on the tube wall can be deduced from the relation $1/f_{IR} = \alpha L_{AFM}/(N_{defect} + 1)$. In Figure 3c, the inverse of the FIR peak position is plotted as a function of L_{AFM} for each synthesis method. Apparently, these curves exhibit linear dependence on L_{AFM}, with different slopes depending on the growth methods. Although zero *x*-intercepts are expected based on the model, these lines showed the finite intercepts. Such finite intercepts may be caused by the nonactive region at the tube edge and/or around the defects of the SWCNT channels. At present, the reasons for the different values of the *x*-intercept among the SWCNTs are unclear.

The intensity ratio of the G mode to the D mode (G/D) in the resonance Raman spectrum has frequently been used to estimate the crystallinity of SWCNTs because the G/D value is closely related to the number of defects and edges.[39] For this purpose, the obtained slopes for each SWCNT were plotted as a function of the G/D values of SWCNTs with the short sonication times (inset of Figure 3c) (also see Supporting Information for details). The higher G/D samples with better crystallinities, such as e-DIPS and arc-SWCNTs, have higher slope values. The good correlation between the slopes and the G/D values suggests that the induced plasmons on SWCNTs resonate with the effective tube length.

If the FIR peak position is related to the effective tube length through the crystallinity of the SWCNT walls, the observed peak positions are expected to be directly correlated with the electric resistances of the SWCNT sample films. Figure 5a shows the *V*–*I* curves of the arc-SWCNT thin films, which were used for the optical measurements. Here, we applied four-probe measurements to avoid contact resistance with same film thickness (250 nm) and annealing conditions. The distance between the probe electrodes was kept constant in all measurements. In fact, the *V*–*I* curve of the four-probe measurements shows better linearity within this applied voltage than that of two-probe

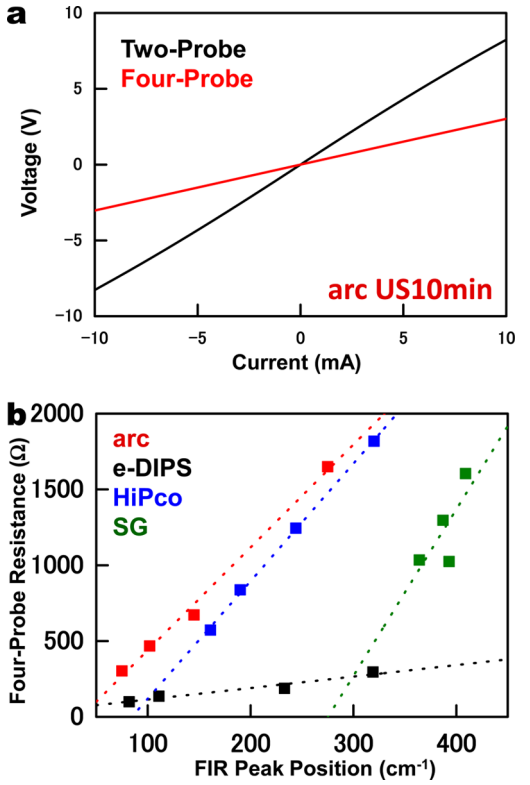

Figure 5. (a) *V*–*I* curves of the arc 10 min sample with two-probe (black) and four-probe (red) measurements. (b) Obtained four-probe resistances as functions of the FIR peak positions.

measurements. As shown in Figure 5b, the SWCNT samples with longer sonication times tended to exhibit high electrical resistance. For example, the arc-SWCNT sample with 10 min sonication shows a resistance of 300 Ω, while a value of 1650 Ω was obtained for arc-SWCNTs that were subjected to 3 h treatment.

The electrical resistance of a SWCNT thin-film sample is influenced by various parameters, including SWCNT length and diameter, the ratio of metallic and semiconducting SWCNTs, doping and adsorption conditions, and geometrical network structures. In the present case, however, almost all parameters remained unchanged following the sonication processes except for the tube length. The increase in resistance is thus attributable to an increase in the number of junctions in the SWCNT network between the source and drain electrodes. All SWCNT samples studied here also exhibited positive correlations between the electrical resistances and the FIR peak positions, that is, the effective tube lengths (Figure 5b). These observations suggest that the FIR signals of SWCNTs originate from the 1D plasmons in the clean nanotube channels and that the current path length determines the observed resonance conditions.

CONCLUSION

In summary, the optical properties of SWCNTs in the FIR frequency region were systematically investigated.

The FIR peak positions shifted toward higher frequencies as the tube lengths were shortened while maintaining constant diameter and chiral-angle distributions of the SWCNTs. The present result strongly suggests that the curvature-induced mini-gap is not responsible for the FIR peaks. The longer and clean SWCNT showed good agreement with 1D plasmon resonance theory in their plasmon dispersion relationship. The chemical-doping studies clearly indicated that the motion of the free carriers on the electronic bands is primarily responsible for the optical response in the FIR region. Because the resonance conditions are disturbed by defects (or kinks) on the tube wall, the observed resonance frequency is closely related to the current path length.

Generally, it is necessary to fabricate an atomic-scale metal wire to observe strong 1D and metallic characteristics because the Fermi wavelength is normally less than 1 nm.[40,41] For instance, Au-induced 1D chain structures on stepped Si(557) surfaces have been found to exhibit characteristic plasmon dispersion, which is expected for a 1D electronic system.[42] However, it has been shown that a SWCNT can be regarded as an ideal 1D system along the direction of its axis.[43] The present observation of a 1D plasmon resonance is also regarded as a "quantum wire" aspect of SWCNTs.

METHODS

Sample Preparation. Four types of SWCNTs were used in the present study: (1) electric arc-produced SWCNTs (APJ, Meijo Nanocarbon Inc.) of 1.2−1.6 nm in diameter (d_t); (2) e-DIPS SWCNTs[44] with d_t = 1.5−2.5 nm; (3) HiPco SWCNTs (CNI Inc.) with d_t = 0.8−1.3 nm; and (4) supergrowth (SG) SWCNTs[45] with d_t = 2−4 nm. The metallic- and semiconducting-enriched arc-SWCNTs were purchased from Meijo Nanocarbon Inc.

The SWCNT samples were cut in water that contained 1 wt % sodium dodecylbenzenesulfonate (SDBS) using a tip-type sonicator (Sonics VCX500, operated at 200 W). The resultant solution was filtered to form a SWCNT thin film, and the thin film was transferred onto high-resistance silicon wafers, which were grown using the floating zone method. These low-carrier-density wafers had a high resistivity of more than 8000 Ω·cm to avoid unexpected absorption in the FIR frequency range because of free-carrier Drude absorptions. To estimate the thickness of the SWCNT thin films, the difference in height between the top of the thin film and the substrate was measured *via* AFM. The estimated thickness was used for the spectral-intensity calibrations.

AFM samples for estimating the length distribution were prepared by dropping the SWCNT-SDBS solutions onto Si substrates. The SDBS deposited on the substrate was rinsed several times with distilled water.

For the chemical-doping experiments, tetrafluorotetracyanoquinodimethane (Tokyo Chemical Industry Co., Ltd.) and tetracyanoquinodimethane (Sigma-Aldrich Co.) were dissolved in acetone (3 and 4 mM, respectively). The solutions were directly dropped onto SWCNT thin-film samples on Si and quartz substrates for the FIR and UV−vis−NIR measurements, respectively, until no further spectral change occurred. Saturated behavior should indicate the full coverage of the SWCNT surface by the adsorbed molecules.

Characterizations. The FIR spectra were measured using an FT-IR spectrometer (Vertex 80v: Bruker Optics) in the 70−8000 cm^{-1} range and a THz-TDS system (TR-1000: Otsuka Electronics) in the 4−70 cm^{-1} range. UV−vis−NIR absorption spectra were measured using UV3100 spectrometers (Shimadzu Inc.). The resonant Raman spectra were measured using a triple-grating T64000 monochromator system (Horiba JY) with diode-pumped solid-state lasers (Spectra Physics) (532 nm). All optical measurements were performed using nonpolar light irradiation. The FIR spectral profile around the peak was fitted by a quadratic polynomial function to obtain the FIR peak position. The sample resistance was measured *via* a four-probe measurement with a constant probe distance on the same samples used in the optical measurements.

All AFM measurements were carried out in tapping mode with Si cantilevers at room temperature (SPM9600: Shimadzu Inc.). Note that small SWCNTs bundles and other small particles still remained even after rinsing. We carefully selected individual SWCNTs that had similar heights to their tube diameters (*e.g.*, approximately 1.2−1.7 nm for the arc-SWCNTs) and then counted the tube lengths to obtain the distribution histograms (Figure 1a and Supporting Information Figures S1a, S3a, and S5a).

Conflict of Interest: The authors declare no competing financial interest.

Acknowledgment. We thank K. Sakai (TASC) for his experimental support. We also thank Dr. T. Nakanishi (AIST) and Professor K. Tominaga (Kobe University) for helpful discussions. This paper is based on results obtained from a project commissioned by the New Energy and Industrial Technology Development Organization (NEDO).

Supporting Information Available: FIR spectroscopic characterization on e-DIPS, HiPco, and supergrowth (SG) SWCNTs, TCNQ doping results on separated arc-SWCNTs, and resonance Raman spectra of SWCNTs in G and D mode regions. This material is available free of charge *via* the Internet at http://pubs.acs.org.

REFERENCES AND NOTES

1. Iijima, S.; Ichihashi, T. Single-Shell Carbon Nanotubes of 1-nm Diameter. *Nature* **1993**, *363*, 603–605.
2. Dresselhaus, M. S., Dresselhaus, G., Avouris, Ph., Eds. *Carbon Nanotubes: Synthesis, Structure, Properties, and Applications* (Topics in Applied Physics 80); Springer-Verlag: Berlin, 2001.
3. Jorio, A., Dresselhaus, G., Dresselhaus, M. S., Eds. *Carbon Nanotubes: Advanced Topics in the Synthesis, Structure, Properties and Applications* (Topics in Applied Physics 111); Springer-Verlag: Berlin, 2008.
4. Kataura, H.; Kumazawa, Y.; Maniwa, Y.; Umezu, I.; Suzuki, S.; Ohtsuka, Y.; Achiba, Y. Optical Properties of Single-Wall Carbon Nanotubes. *Synth. Met.* **1999**, *103*, 2555–2558.
5. Lauret, J.-S.; Voisin, C.; Cassabois, G.; Delalande, C.; Roussignol, Ph.; Jost, O.; Capes, L. Ultrafast Carrier Dynamics in Single-Wall Carbon Nanotubes. *Phys. Rev. Lett.* **2003**, *90*, 057404.
6. Landi, B. J.; Ruf, H. J.; Evans, C. M.; Cress, C. D.; Raffaelle, R. P. Purity Assessment of Single-Wall Carbon Nanotubes, Using Optical Absorption Spectroscopy. *J. Phys. Chem. B* **2005**, *109*, 9952–9965.
7. Itkis, M. E.; Niyogi, S.; Meng, M. E.; Hamon, M. A.; Hu, H.; Haddon, R. C. Spectroscopic Study of the Fermi Level Electronic Structure of Single-Walled Carbon Nanotubes. *Nano Lett.* **2002**, *2*, 155–159.
8. Jeon, T. I.; Kim, K. J.; Kang, C.; Maeng, I. H.; Son, J. H.; An, K. H.; Lee, J. Y.; Lee, Y. H. Optical and Electrical Properties of Preferentially Anisotropic Single-Walled Carbon Nanotube Films in Terahertz Region. *J. Appl. Phys.* **2004**, *95*, 5736.
9. Akima, N.; Iwasa, Y.; Brown, S.; Barbour, A. M.; Cao, J.; Musfeldt, J. L.; Matsui, H.; Toyota, N.; Shiraishi, M.;

Shimoda, H.; *et al.* Strong Anisotropy in the Far-Infrared Absorption Spectra of Stretch-Aligned Single-Walled Carbon Nanotubes. *Adv. Mater.* **2006**, *18*, 1166–1169.
10. Borondics, F.; Kamaras, K.; Nikolou, M.; Tanner, D. B.; Chen, Z. H.; Rinzler, A. G. Charge Dynamics in Transparent Single Walled Carbon Nanotube Films from Optical Transmission Measurements. *Phys. Rev. B* **2006**, *74*, 045431.
11. Kampfrath, T.; von Volkmann, K.; Aguirre, C. M.; Desjardins, P.; Martel, R.; Krenz, M.; Frischkorn, C.; Wolf, M.; Perfetti, L. Mechanism of the Far-Infrared Absorption of Carbon-Nanotube Films. *Phys. Rev. Lett.* **2008**, *101*, 267403.
12. Nakanishi, T.; Ando, T. Optical Response of Finite-Length Carbon Nanotubes. *J. Phys. Soc. Jpn.* **2009**, *78*, 114708.
13. Slepyan, G. Y.; Shuba, M. V.; Maksimenko, S. A.; Thomsen, C.; Lakhtakia, A. Terahertz Conductivity Peak in Composite Materials Containing Carbon Nanotubes: Theory and Interpretation of Experiment. *Phys. Rev. B* **2010**, *81*, 205423.
14. Thirunavukkuarasu, K.; Hennrich, F.; Kamaras, K.; Kuntscher, C. A. Infrared Spectroscopic Studies on Unoriented Single Walled Carbon Nanotube Films under Hydrostatic Pressure. *Phys. Rev. B* **2010**, *81*, 045424.
15. Pekker, A.; Kamaras, K. Wide-Range Optical Studies on Various Single Walled Carbon Nanotubes, Origin of the Low Energy Gap. *Phys. Rev. B* **2011**, *84*, 075475.
16. Ichida, M.; Saito, S.; Nakano, T.; Feng, Y.; Miyata, Y.; Yanagi, K.; Kataura, H.; Ando, H. Absorption Spectra of High Purity Metallic and Semiconducting Single-Walled Carbon Nanotube Thin Films in a Wide Energy Region. *Solid State Commun.* **2011**, *151*, 1696–1699.
17. Shuba, M. V.; Paddubskaya, A. G.; Plyushch, A. O.; Kuzhir, P. P.; Slepyan, G. Y.; Maksimenko, S. A.; Ksenevich, V. K.; Buka, P.; Seliuta, D.; Kasalynas, I.; *et al.* Experimental Evidence of Localized Plasmon Resonance in Composite Materials Containing Single Wall Carbon Nanotubes. *Phys. Rev. B* **2012**, *85*, 165435.
18. Ren, L.; Zhang, Q.; Pint, C. L.; Wójcik, A. K.; Bunney, M., Jr.; Arikawa, T.; Kawayama, I.; Tonouchi, M.; Hauge, R. H.; Belyanin, A. A.; *et al.* Collective Antenna Effects in the Terahertz and Infrared Response of Highly Aligned Carbon Nanotube Arrays. *Phys. Rev. B* **2013**, *87*, 161401R.
19. Zhang, Qi.; Hároz, E. H.; Jin, Z.; Ren, L.; Wang, X.; Arvidson, R. S.; Lüttge, A.; Kono, J. Plasmonic Nature of the Terahertz Conductivity Peak in Single-Wall Carbon Nanotubes. *Nano Lett.* **2013**, *13*, 5991–5996.
20. Ugawa, A.; Rinzler, A. G.; Tanner, D. B. Far-Infrared Gaps in Single-Wall Carbon Nanotubes. *Phys. Rev. B* **1999**, *60*, R11305–R11308.
21. Ouyang, M.; Huang, J.-L.; Cheung, C. L.; Lieber, C. M. Energy Gaps in Metallic Single-Walled Carbon Nanotubes. *Science* **2001**, *292*, 702–705.
22. Hamada, N.; Sawada, S.; Oshiyama, A. New One-Dimensional Conductors: Graphitic Microtubules. *Phys. Rev. Lett.* **1992**, *68*, 1579–1581.
23. Kane, C. L.; Mele, E. J. Size, Shape, and Low Energy Electronic Structure of Carbon Nanotubes. *Phys. Rev. Lett.* **1997**, *78*, 1932–1935.
24. Mintmire, J. W.; White, C. T. Universal Density of States for Carbon Nanotubes. *Phys. Rev. Lett.* **1998**, *81*, 2506–2509.
25. Ju, L.; Geng, B.; Horng, J.; Girit, C.; Martin, M.; Hao, Z.; Bechtel, H. A.; Liang, X.; Zettl, A.; Shen, Y. R.; *et al.* Graphene Plasmonics for Tunable Terahertz Metamaterials. *Nat. Nanotechnol.* **2011**, *6*, 630–634.
26. Freitag, M.; Low, T.; Zhu, W.; Yan, H.; Xia, F.; Avouris, P. Photocurrent in Graphene Harnessed by Tunable Intrinsic Plasmons. *Nat. Commum.* **2013**, *4*, 1951.
27. Yan, H.; Low, T.; Zhu, W.; Wu, Y.; Freitag, M.; Li, X.; Guinea, F.; Avouris, P.; Xia, F. Damping Pathways of Mid-infrared Plasmons in Graphene Nanostructures. *Nat. Photonics* **2013**, *7*, 394–399.
28. Sarma, S. D.; Hwang, E. H. Collective Modes of the Massless Dirac Plasma. *Phys. Rev. Lett.* **2009**, *102*, 206412.
29. Rao, A. M.; Richter, E.; Bandow, S.; Chase, B.; Eklund, P. C.; Williams, K. A.; Fang, S.; Subbaswamy, K. R.; Menon, M.; Thess, A.; *et al.* Diameter-Selective Raman Scattering from Vibrational Modes in Carbon Nanotubes. *Science* **1997**, *275*, 187–191.
30. Liang, W.; Bockrath, M.; Bozovic, D.; Hafner, J. H.; Tinkham, M.; Park, H. Fabry-Perot Interference in a Nanotube Electron Waveguide. *Nature* **2001**, *411*, 665–669.
31. Cho, K. Nonlocal Theory of Radiation–Matter Interaction: Boundary-Condition-Less Treatment of Maxwell Equations. *Prog. Theor. Phys. Suppl.* **1991**, *106*, 225–233.
32. Kramberger, C.; Hambach, R.; Giorgetti, C.; Rümmeli, M. H.; Knupfer, M.; Fink, J.; Büchner, B.; Reining, L.; Einarsson, E.; Maruyama, S.; *et al.* Linear Plasmon Dispersion in Single-Wall Carbon Nanotubes and the Collective Excitaion Spectrum of Graphene. *Phys. Rev. Lett.* **2008**, *100*, 196803.
33. Nagao, T.; Hildebrandt, T.; Henzler, M.; Hasegawa, S. Dispersion and Damping of a Two-Dimensional Plasmon in a Metallic Surface-State Band. *Phys. Rev. Lett.* **2001**, *86*, 5747–5750.
34. Takenobu, T.; Takano, T.; Shiraishi, M.; Murakami, Y.; Ata, M.; Kataura, H.; Achiba, Y.; Iwasa, Y. Stable and Controlled Amphoteric Doping by Encapsulation of Organic Molecules Inside Carbon Nanotubes. *Nat. Mater.* **2003**, *2*, 683–688.
35. Kazaoui, S.; Minami, N.; Jacquemin, R.; Kataura, H.; Achiba, Y. Amphoteric Doping of Single-Wall Carbon Nanotube Thin Films As Probed by Optical Absorption Spectroscopy. *Phys. Rev. B* **1999**, *60*, 13339–13342.
36. Dyakonov, M.; Shur, M. Shallow Water Analogy for Ballistic Field Effect Transistor: New Mechanism of Plasma Wave Generation by dc Current. *Phys. Rev. Lett.* **1993**, *71*, 2465–2468.
37. Dyer, G. C.; Vinh, N. Q.; Allen, S. J.; Aizin, G. R.; Mikalopas, J.; Reno, J. L.; Shaner, E. A. A Terahertz Plasmon Cavity Detector. *Appl. Phys. Lett.* **2010**, *97*, 193507.
38. Dyer, G. C.; Preu, S.; Aizin, G. R.; Mikalopas, J.; Grine, A. D.; Reno, J. L.; Hensley, J. M.; Vinh, N. Q.; Gossard, A. C.; Sherwin, M. S.; *et al.* Enhanced Performance of Resonant Sub-terahertz Detection in a Plasmonic Cavity. *Appl. Phys. Lett.* **2012**, *100*, 083506.
39. Miyata, Y.; Mizuno, K.; Kataura, H. Purity and Defect Characterization of Single-Wall Carbon Nanotubes Using Raman Spectroscopy. *J. Nanomater.* **2011**, *2011*, 786763.
40. Segovia, P.; Purdie, D.; Hengsberger, M.; Baer, Y. Observation of Spin and Charge Collective Modes in One-Dimensional Metallic Chains. *Nature* **1999**, *402*, 504–507.
41. Losio, R.; Altmann, K. N.; Kirakosian, A.; Lin, J.-L.; Petrovykh, D. Y.; Himpsel, F. J. Band Splitting for Si(557)–Au: Is It Spin-Charge Separation? *Phys. Rev. Lett.* **2001**, *86*, 4632–4635.
42. Nagao, T.; Yaginuma, S.; Inaoka, T.; Sakurai, T. One-Dimensional Plasmon in an Atomic-Scale Metal Wire. *Phys. Rev. Lett.* **2006**, *97*, 116802.
43. Ishii, H.; Kataura, H.; Shiozawa, H.; Yoshioka, H.; Otsubo, H.; Takayama, Y.; Miyahara, T.; Suzuki, S.; Achiba, Y.; Nakatake, M.; *et al.* Direct Observation of Tomonaga Luttinger-Liquid State in Carbon Nanotubes at Low Temperatures. *Nature* **2003**, *426*, 540–544.
44. Saito, T.; Ohshima, S.; Okazaki, T.; Ohmori, S.; Yumura, M.; Iijima, S. Selective Diameter Control of Single-Walled Carbon Nanotubes in the Gas-Phase Synthesis. *J. Nanosci. Nanotechnol.* **2008**, *8*, 6153–6157.
45. Hata, K.; Futaba, D. N.; Mizuno, K.; Namai, T.; Yumura, M.; Iijima, S. Water-Assisted Highly Efficient Synthesis of Impurity-Free Single-Walled Carbon Nanotubes. *Science* **2004**, *306*, 1362–1364.